

## All paths lead to hubs in the spectroscopic networks of water isotopologues $\text{H}_2^{16}\text{O}$ and $\text{H}_2^{18}\text{O}$

Roland Tóbiás <sup>1</sup>, Meissa L. Diouf <sup>2</sup>, Frank M. J. Cozijn <sup>2</sup>, Wim Ubachs <sup>2</sup>✉ & Attila G. Császár <sup>1</sup>✉

Network theory has fundamentally transformed our comprehension of complex systems, catalyzing significant advances across various domains of science and technology. In spectroscopic networks, hubs are the quantum states involved in the largest number of transitions. Here, utilizing network paths probed via precision metrology, absolute energies have been deduced, with at least 10-digit accuracy, for almost 200 hubs in the experimental spectroscopic networks of  $\text{H}_2^{16}\text{O}$  and  $\text{H}_2^{18}\text{O}$ . These hubs, lying on the ground vibrational states of both species and the bending fundamental of  $\text{H}_2^{16}\text{O}$ , are involved in tens of thousands of observed transitions. Relying on the same hubs and other states, benchmark-quality line lists have been assembled, which supersede and improve, by three orders of magnitude, the accuracy of the massive amount of data reported in hundreds of papers dealing with Doppler-limited spectroscopy. Due to the omnipresence of water, these ultraprecise line lists could be applied to calibrate high-resolution spectra and serve ongoing and upcoming space missions.

<sup>1</sup>Laboratory of Molecular Structure and Dynamics, Institute of Chemistry, ELTE Eötvös Loránd University and HUN-REN-ELTE Complex Chemical Systems Research Group, H-1117 Budapest, Pázmány Péter sétány 1/A, Hungary. <sup>2</sup>Department of Physics and Astronomy, LaserLaB, Vrije Universiteit, De Boelelaan 1081, 1081 HV Amsterdam, The Netherlands. ✉email: [w.m.g.ubachs@vu.nl](mailto:w.m.g.ubachs@vu.nl); [attila.csaszar@ttk.elte.hu](mailto:attila.csaszar@ttk.elte.hu)

Network theory<sup>1</sup>, a branch of discrete mathematics useful to investigate large natural and artificial systems, has experienced rapid development and widespread applications over the last two decades<sup>2,3</sup>. In fact, network-based analysis of complex systems, including social communities<sup>4</sup>, ecological associations<sup>5</sup>, cancer genomes<sup>6</sup>, brain connectomes<sup>7</sup>, as well as the COVID-19 pandemic<sup>8,9</sup>, has been a hot topic in contemporary interdisciplinary research. Common to these complex systems is that their representation with a network brings considerable advantages during the exploration of their intrinsic properties. In these large-scale networks, the degrees of the nodes often display an inverse-power-law-like (i.e., heavy-tailed or nearly scale-free<sup>2,10,11</sup>) distribution, indicating the presence of a limited number of unusually high-degree nodes, called hubs (note that the degree of a node is the number of edges attached to it).

More than a decade and a half ago, network theory found its way into high-resolution molecular spectroscopy, as well<sup>12,13</sup>. In a spectroscopic network (SN), the nodes are quantum states and the edges are lines/transitions among these states (unless otherwise noted, the words “line” and “transition” refer here to a one-photon, electric-dipole-allowed rovibrational line, though SNs may also contain other types of transitions). According to the Ritz principle<sup>14</sup>, a transition frequency is proportional to the energy difference of the upper and lower states, allowing the determination of empirical energies from a set of measured line positions.

Due to their outstanding significance in numerous scientific and engineering applications (e.g., astronomy, atmospheric sensing, radiative transfer, and combustion chemistry), information related to experimental and/or computed transitions are collated into large-scale, line-by-line spectroscopic datasets, such as those forming the basis of the HITRAN database<sup>15</sup>. As shown repeatedly<sup>13,16–21</sup>, network theory offers a powerful instrument for the maintenance of these databanks, with the unique ability to analyze the self-consistency of the transitions deposited<sup>16,18,19,21</sup>.

Experimental SNs, that is networks built upon measured transitions, possess a heavy-tailed degree distribution<sup>13,16</sup>. This does not hold for SNs formed by complete theoretical line lists, but once lines below an experimentally reasonable detection limit are excluded, their degree distribution becomes heavy-tailed. Since hubs are typically the lower states in a vast number of lines, the accurate knowledge of their energies is of paramount importance when deriving accurate upper-state energies, for example, through the use of the combination-difference approach popular among spectroscopists.

When pursuing high accuracy, modern precision-spectroscopy techniques<sup>22–32</sup>, which often rely on frequency combs and cavity enhancement under non-linear (Doppler-free) absorption conditions, are extremely valuable as they allow to lower the frequency uncertainties down to the kHz level. This high accuracy is helpful in a wide range of applications, like frequency metrology<sup>26,31</sup>, assessing the time stability of physical constants<sup>33</sup>, searching for new physics beyond the standard model<sup>34</sup>, and analyzing velocity fields in star-forming regions<sup>35</sup>.

In this article, the spectral hubs of H<sub>2</sub><sup>16</sup>O and H<sub>2</sub><sup>18</sup>O, the two most abundant water isotopologues, are scrutinized via spectroscopic-network-assisted precision spectroscopy (SNAPS)<sup>36</sup>. For these astronomically and atmospherically relevant triatomic molecules, the energies of the hubs are ascertained from well-designed network paths (i.e., sequences of connected, unrepeated transitions and states). These paths involve Lamb-dip lines yielded by this study or collected from the literature<sup>36–41</sup>. The set of transitions targeted for measurement is composed via an inventive design scheme and the Lamb dips are detected with two<sup>26,32</sup> noise-immune cavity-enhanced optical heterodyne molecular spectroscopy (NICE-OHMS)<sup>22,23</sup> setups equipped with three probe lasers.

## Results and discussion

**Identification of hubs in the H<sub>2</sub><sup>16</sup>O and H<sub>2</sub><sup>18</sup>O networks.** Let us first define what a spectral hub is, as there is no strict definition for hubs in network theory<sup>1</sup>. Our definition followed in this study is that a hub is a state with degree  $d \geq d^*$ , where  $d^*$  is the largest integer for which at least 1 % of the states have at least  $d^*$  edges.

Figure 1 shows the degree distribution in the experimental H<sub>2</sub><sup>16</sup>O network<sup>42</sup>, where all but one of the 182 hubs correspond to the  $P=0$  and  $P=1$  polyads, that is to the ground vibrational state, (0 0 0), and the bend fundamental, (0 1 0), respectively. The single exception is a highly excited rovibrational state of the  $P=16$  polyad, which appears rather unexpectedly in the list of hubs; its occurrence is due to the large number of transitions reported in ref. <sup>43</sup>. Of the other 181 hubs, 149 and 32 lie on the  $P=0$  and  $P=1$  polyads, respectively. As to the experimental SN of H<sub>2</sub><sup>18</sup>O<sup>42</sup>, it is characterized by a degree distribution similar to that of Fig. 1a (see Supplementary Data 1). The 6755 states linked by purely experimental lines define 68 hubs, all within the  $P=0$  polyad.

An important goal of this study is to determine highly accurate energies for (a) all the H<sub>2</sub><sup>18</sup>O hubs and (b) a large number of H<sub>2</sub><sup>16</sup>O hubs, including all the  $P=1$  hubs. Achieving these objectives strongly relies on recent instrumental developments in our precision-spectroscopy apparatus<sup>32</sup> and an innovative network-based design scheme described in the following subsection.

**Network-guided precision measurements.** Figure 2 demonstrates an elaborate network-based design scheme constructed to provide ultraprecise energies for the hubs of H<sub>2</sub><sup>16</sup>O and H<sub>2</sub><sup>18</sup>O, making use of the three laser ranges accessible in our two NICE-OHMS setups. Figure 2a displays two highly-connected clusters, distinguished by their lower states belonging either to the  $P=0$  or  $P=1$  polyad. For one-photon, dipole-allowed  $P'_{4/5} \leftarrow P''_{0/1}$  transitions, such as those measured here, both the  $P=0$  and the  $P=1$  clusters are disconnected subnetworks. To join the even-parity  $P=0$  and  $P=1$  states with their odd-parity counterparts, a few pure rotational  $P'_0 \leftarrow P''_0$  and  $P'_1 \leftarrow P''_1$  lines should be included in both clusters. A way to make connections between the  $P=0$  and  $P=1$  states is to concatenate the two clusters with  $\Lambda$  pairs of  $P'_5 \leftarrow P''_0$  transitions lying within the range of Laser III (a  $\Lambda$ -pair is formed by two lines sharing the same upper state). Connectivity inside the *ortho* and *para* subnetworks could be secured without reliance on less accurate (~30–300 kHz), far-infrared  $P'_0 \leftarrow P''_0$  and  $P'_1 \leftarrow P''_1$  transitions, introducing a handful of  $P'_5 \leftarrow P''_0$  lines into the network.

Due to the absence of observed *ortho* ↔ *para* lines<sup>44,45</sup>, the *ortho* and *para* subnetworks are two separate components (i.e., maximal connected collections of states), preventing the overall experimental connection of the Fig. 2a network. Thus, only relative *ortho* energies can be obtained from the experiments, where the relative energy of an *ortho/para* state is specified as the difference between the absolute energy of this state and that of the lowest-energy *ortho/para* state. For the empirical derivation of absolute *ortho* energies, one could (i) employ accurate theoretical *ortho–para* splittings<sup>36,40</sup> by creating artificial links between the two components or (ii) add the lowest *ortho* energy of an effective Hamiltonian model to the relative values. In what follows, option (ii) is applied.

To explicate and contextualize Fig. 2a, paths involving the four lowest-lying  $P=1$  states are depicted in Fig. 2b. The top two lines of the four paths are  $\Lambda$  pairs and these pairs introduce links between the sets of  $P=0$  and  $P=1$  states. The bottom parts of these paths are also useful, as they illustrate how the (*ortho/para*, *even/odd*) states of the  $P=0$  polyad can be attained via



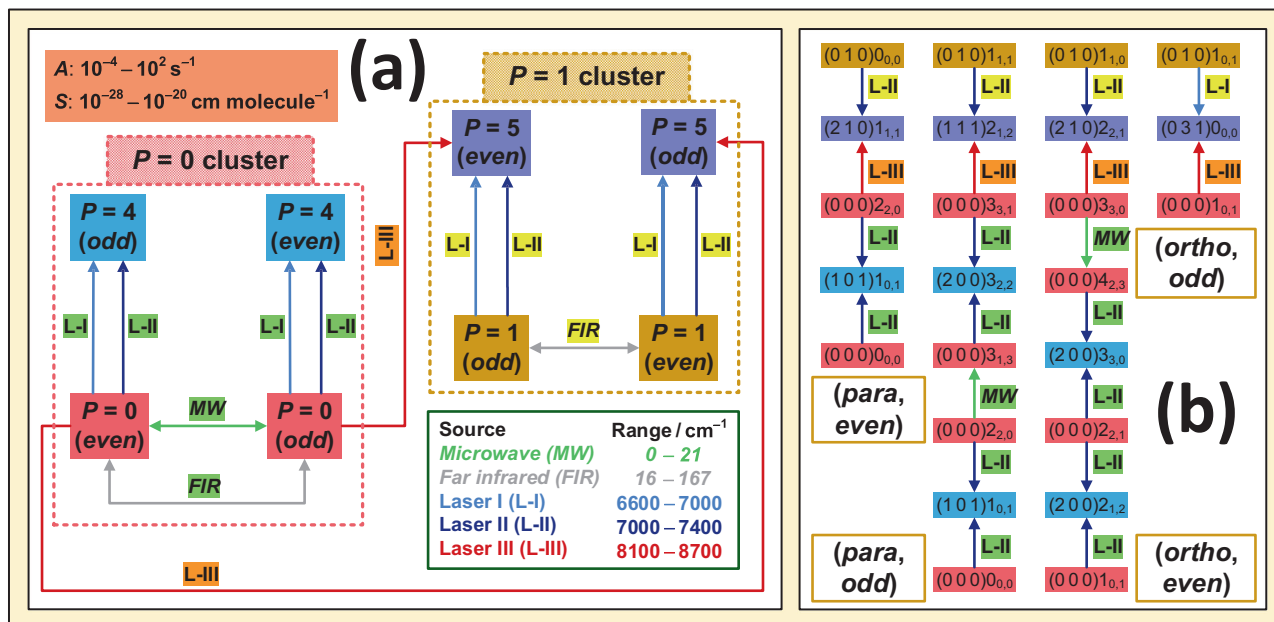


**Fig. 2** Design scheme used for the precise characterization of hubs in the  $\text{H}_2^{16}\text{O}$  and  $\text{H}_2^{18}\text{O}$  networks. For the general terms and spectroscopic symbols employed, see the central panel of Fig. 1. The colors of the transitions denoted with arrows are shown in a green-framed box collecting the wavenumber ranges of the probe lasers. The apricot box exhibits the Einstein-A coefficient and the room-temperature intensity windows accessible in the intervals of the L-I, L-II, and L-III lasers. The highly accurate green and the less accurate gray transitions are taken from refs. 37–39,53,54, whereas the light blue, dark blue, and brick-red lines were targeted during this study and in refs. 36,40, and 41. Panel **a** shows the network-based design scheme, whereby the even/odd-parity states of the  $P=0$ ,  $P=1$ ,  $P=4$ , and  $P=5$  polyads are represented with red, brown, cerulean blue, and lavender blue boxes, respectively. Panel **b** gives examples for paths securing uninterrupted connections from the  $(0\ 1\ 0)_{J \leq 1}_{k_c, k_c}$  states to the *para* and *ortho* rovibrational ground states,  $(0\ 0\ 0)_{0,0,0}$  and  $(0\ 0\ 0)_{1,0,1}$ , respectively.

Utilizing our NICE-OHMS setups and the list of targeted transitions, 135/7 absorption lines were observed under saturation for  $\text{H}_2^{16}\text{O}/\text{H}_2^{18}\text{O}$  (see also Fig. 3 and Table 1). These Lamb dips are characterized by diverse linewidths (half-width at half maximum) of 150–1500 kHz, when measured at room temperature (296 K), a total sample pressure of 0.05–0.55 Pa, and an intracavity power of 1–100 W. The collection of new transitions includes 8, 117, and 17 lines in the regions of Lasers I, II, and III, respectively (see Fig. 2). For all these transitions, line-by-line uncertainties were ascertained. In the case of five  $\text{H}_2^{16}\text{O}$  lines, the pressure shifts were studied explicitly, with the result that all slopes fall within  $\pm 20$  kHz Pa<sup>-1</sup>, the highest value found earlier<sup>36,40,41</sup>. The experimental line positions, along with their calculated  $1\sigma$  uncertainties, are deposited in Supplementary Data 1.

**Ultrahigh-accuracy absolute rovibrational energies.** From the dataset of newly determined Lamb-dip lines and those high-accuracy transitions reported in refs. 36–41 and 46–48, two ultraprecise SNs were built. The  $\text{H}_2^{16}\text{O}/\text{H}_2^{18}\text{O}$  SNs are formed by 397/208 lines and 317/195 states, forming two (principal) components based on nuclear-spin statistics. Setting the squared line uncertainties as edge weights, a shortest-path search<sup>1</sup> was carried out from the *ortho/para* ground state to the other *ortho/para* states. The resulting paths are named here best paths, as they produce the best relative energies and associated uncertainties for their terminal states.

Figure 4 illustrates two disjoint paths,  $p_1$  and  $p_2$ , for the highest-degree  $P=1$  hub of  $\text{H}_2^{16}\text{O}$ , together with the Lamb-dip spectra of two typical lines on  $p_1$ . These two paths specify a cycle (that is a series of connected lines and states, where each state has exactly two neighboring states), whose discrepancy satisfies Eq. (5) of the Methods section, corroborating the high accuracy of the underlying transitions. The two paths provide basically the same relative energies, of which the lower-uncertainty datum is adopted as the

final estimate. It is worth emphasizing that the average uncertainty of the relative energies is around  $3.5 \times 10^{-7}$  cm<sup>-1</sup> in the ultraprecise  $\text{H}_2^{16}\text{O}/\text{H}_2^{18}\text{O}$  SNs, implying a 10–1000 times improvement over previous, Doppler-limited measurement results.

To switch to absolute energies, the relative *ortho* energies need to be shifted with the lowest *ortho*- $\text{H}_2^{16}\text{O}$  and *ortho*- $\text{H}_2^{18}\text{O}$  energy, determined to be 23.794 361 22(25)<sup>36</sup> and 23.754 904 61(19) cm<sup>-1</sup><sup>40</sup>, respectively. After this conversion, accurate absolute energies could be derived for 55/100 % of the hubs in the  $P=0$  polyad of  $\text{H}_2^{16}\text{O}/\text{H}_2^{18}\text{O}$ , as well as for all the  $P=1$  hubs of  $\text{H}_2^{16}\text{O}$ . Thus, 115/68 of the  $\text{H}_2^{16}\text{O}/\text{H}_2^{18}\text{O}$  hubs are now known with an accuracy of a few times  $10^{-7}$  cm<sup>-1</sup>, which are incident to 31 204/14 637 unique transitions inside the experimental  $\text{H}_2^{16}\text{O}/\text{H}_2^{18}\text{O}$  networks (see Supplementary Data 1). Furthermore, the new measurements appended altogether 61 states of the  $P=1$  polyad to the ultraprecise  $\text{H}_2^{16}\text{O}$  network, representing a complete set up to  $J=6$  and delivering an improved estimate, 1 594.746 272 93(25) cm<sup>-1</sup>, for the bending fundamental of  $\text{H}_2^{16}\text{O}$ . For both  $\text{H}_2^{16}\text{O}$  and  $\text{H}_2^{18}\text{O}$ , the best paths, together with the ultrahigh-accuracy energies and their uncertainties, are available in Supplementary Data 1.

**Ultraprecise reference line lists.** Exploiting the ultraprecise paths composed during this study, the benchmark-quality predicted line lists of  $\text{H}_2^{16}\text{O}$ <sup>41</sup> and  $\text{H}_2^{18}\text{O}$ <sup>40</sup> have been enlarged significantly. In the updated lists, a transition is represented with a differential path, which can be generated from the disjoint lines of the two best paths visiting the upper and lower states. These differential paths yield the transition wavenumbers and kHz-level uncertainties for the predicted lines. The updated line lists of  $\text{H}_2^{16}\text{O}/\text{H}_2^{18}\text{O}$ , placed in Supplementary Data 1, include 4742/1690 entries, out of which 1907/878 lines have relatively high intensity,  $S \geq 10^{-25}$  cm molecule<sup>-1</sup>. These ultraprecise databases span the 0–3868/0–1249



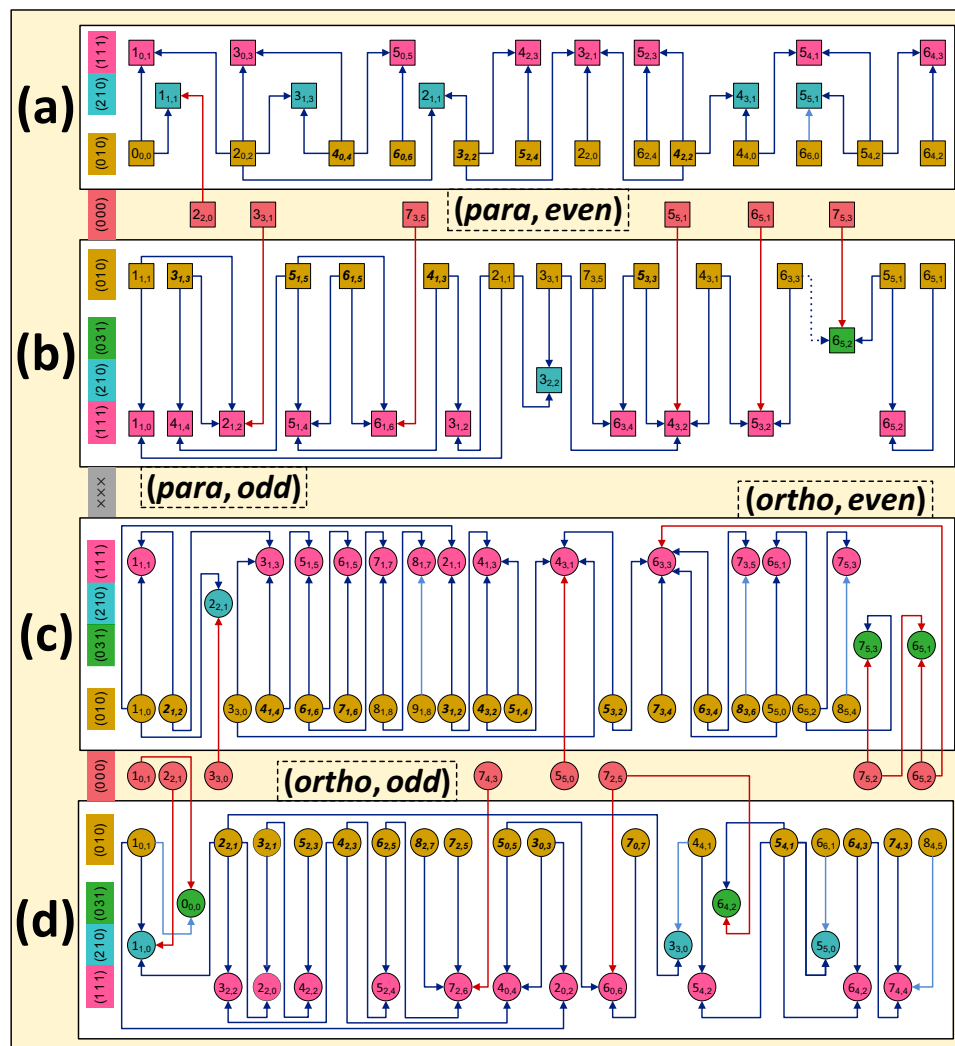


**Fig. 3 Pictorial overview of the precision lines detected during this study for the  $\text{H}_2^{16}\text{O}$  isotopologue.** For the general notions and symbols employed, consult the central panel of Fig. 1. In this actual figure, the *ortho* and *para* states are marked with circles and squares, respectively. For all these states, the  $J_{K_a, K_c}$  assignments are written out explicitly, whereas the  $(v_1, v_2, v_3)$  triplets are given in the left-side color legend. Those states with rotational labels typeset in bold italics are hubs within the degree distribution of Fig. 1a. The arrows, whose colors are specified in the green box of Fig. 2a, mean transitions measured during this study with an accuracy of 1.9–38.8 kHz. To the best of our knowledge, the dotted  $(0\ 3\ 1)6_{5,2} \leftarrow (0\ 1\ 0)6_{3,3}$  line, see panel **b**, is the least intense ( $S = 4.9 \times 10^{-28}$  cm molecule $^{-1}$ ) transition that has ever been identified for water isotopologues in saturation. Drawing on the *even/odd* and *ortho/para* labels of the lower states, the blue lines can be divided into four internally connected subnetworks (see panels **a–d**). These subnetworks are linked to some  $P = 0$  states through the brick-red lines. Albeit not indicated, these  $P = 0$  states are joined via ultraprecise paths, shown in Figs. 3 and 4 of ref. <sup>41</sup>, to the *ortho/para* ground state.

and 4430–12666/5909–8379  $\text{cm}^{-1}$  wavenumber ranges, and have 2328/822 and 2414/868 lines, respectively.

The high-intensity transitions of the lower wavenumber interval represent  $P'_0 \leftarrow P''_0$ ,  $P'_1 \leftarrow P''_0$ , and  $P'_1 \leftarrow P''_1$  lines, of which the latter two stem from our newly measured  $\text{H}_2^{16}\text{O}$  transitions. A great number of these  $P'_{0/1} \leftarrow P''_{0/1}$  lines establish links between pairs of hubs (see, e.g., the connections of the middle state with a few yellow states in Fig. 1b). Similar to social networks<sup>10</sup>, the hubs of the experimental  $\text{H}_2^{16}\text{O}$  and  $\text{H}_2^{18}\text{O}$  SNs are also highly interconnected, due to preferential attachment driven by quantum-mechanical selection rules<sup>16</sup>.

While our line catalogs contain only one-photon transitions allowed by dipole and nuclear-spin selection rules, other types of extremely weak lines, like two-photon, quadrupole, and *ortho-para* transitions, could also be deduced with 10–20 kHz uncertainties from the accurate absolute energies. It must be stressed that

measuring quadrupole and/or two-photon  $P'_{4/5} \leftarrow P''_{0/1}$  lines based on these accurate predictions would be truly advantageous, as they could ensure stronger connections between the loosely attached *even-* and *odd-*parity  $P_{0/1}$  states.

### Concluding remarks

An important message of this study is that combining network theory with precision spectroscopy provides an outstanding tool for the ultraprecise characterization of hubs, the most relevant quantum states in an experimental spectroscopic network. In fact, utilization of a sophisticated design scheme and the detection of close to 150 new Lamb dips for  $\text{H}_2^{16}\text{O}$  and  $\text{H}_2^{18}\text{O}$  resulted in absolute energies with a typical relative accuracy of  $10^{-10}$  for the complete set of  $\text{H}_2^{18}\text{O}$  hubs, as well as for all the  $\text{H}_2^{16}\text{O}$  hubs on the bending fundamental and a large part of the hubs within its ground vibrational state. To access the remaining  $\text{H}_2^{16}\text{O}$  hubs with ultrahigh accuracy, further

**Table 1** Ultrahigh-accuracy results obtained during this study for the H<sub>2</sub><sup>18</sup>O isotopologue<sup>a</sup>.

Transition (NICE-OHMS)		Lower state (SNAPS)		
Pair	Assignment	Wavenumber/cm <sup>-1</sup>	Relative energy/cm <sup>-1</sup>	Hub?
1 & 2	(2 0 0) <sub>8<sub>3,6</sub></sub> ← (0 0 0) <sub>8<sub>2,7</sub></sub>	<b>7267.323 965 992(67)</b>	858.159 130 38(19)	yes
	(2 0 0) <sub>8<sub>3,6</sub></sub> ← (0 0 0) <sub>9<sub>0,9</sub></sub>	<b>7232.980 364 473(83)</b>	<b>892.502 731 90(21)</b>	yes
3 & 4	(1 0 1) <sub>8<sub>3,5</sub></sub> ← (0 0 0) <sub>8<sub>3,6</sub></sub>	<b>7237.244 485 887(67)</b>	977.950 777 34(28)	yes
	(1 0 1) <sub>8<sub>3,5</sub></sub> ← (0 0 0) <sub>9<sub>1,8</sub></sub>	<b>7164.187 247 276(83)</b>	<b>1051.008 015 95(30)</b>	yes
5 & 6	(0 0 2) <sub>8<sub>3,6</sub></sub> ← (0 0 0) <sub>8<sub>4,5</sub></sub>	<b>7270.314 091 144(87)</b>	1092.881 155 49(24)	yes
	(0 0 2) <sub>8<sub>3,6</sub></sub> ← (0 0 0) <sub>9<sub>2,7</sub></sub>	<b>7188.750 644 337(83)</b>	<b>1174.444 602 30(27)</b>	yes
7 & 8	(2 0 0) <sub>9<sub>5,4</sub></sub> ← (0 0 0) <sub>8<sub>6,3</sub></sub>	7197.666 239 152(77)	1375.672 914 85(35)	no
	(2 0 0) <sub>9<sub>5,4</sub></sub> ← (0 0 0) <sub>9<sub>4,5</sub></sub>	<b>7241.894 981 064(87)</b>	<b>1331.444 172 94(36)</b>	yes

<sup>a</sup> Columns 1–3 contain the transitions probed with our NICE-OHMS spectrometers to produce new SNAPS-based energies for four H<sub>2</sub><sup>18</sup>O hubs. Column 4 comprises the relative energies of the lower states derived via the SNAPS method. Column 5 lists which of the lower states are hubs in the experimental H<sub>2</sub><sup>18</sup>O network (see Supplementary Data 1). All numerical data typeset in boldface are results of the present study, whereas the plain values are taken from ref. 40. The transition wavenumbers and the relative energies are associated with the 1 $\sigma$  uncertainties of their last digits in parentheses. The lines of this table form  $\Lambda$  pairs, whose wavenumber differences yield energy differences for their lower states. For each  $\Lambda$  pair, the boldfaced relative energy can be reproduced by forming the sum of the associated wavenumber difference and the other (plain) relative energy. The uncertainties of the relative energies are combined 1 $\sigma$  uncertainties (i.e., the square roots of the sum-of-squared uncertainties).

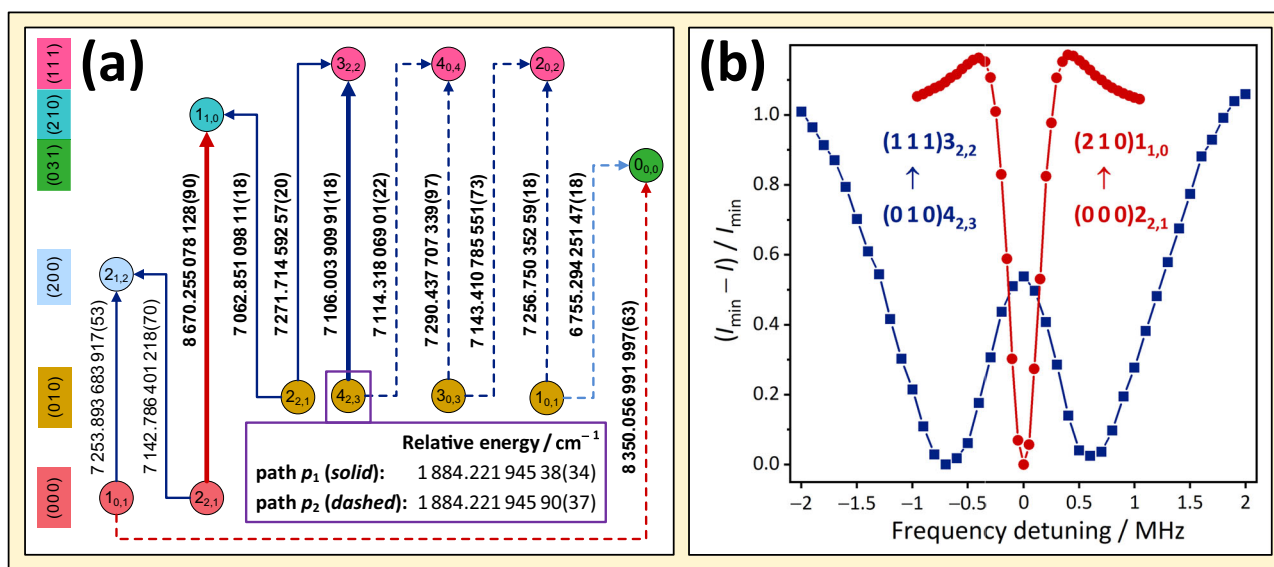


**Fig. 4** Illustration of the SNAPS procedure in operation for the highest-degree  $P = 1$  hub of H<sub>2</sub><sup>16</sup>O. The general terms and symbols utilized are defined in the central panel of Fig. 1. Panel **a** contains two disjoint paths from (0 0 0)<sub>10,1</sub> to (0 1 0)<sub>42,3</sub>,  $p_1$  and  $p_2$ , where the lines are denoted with solid and dashed arrows, respectively. For the transitions and the states of panel **a**, the same formalism is adopted as in Fig. 3. The numbers on the arrows are wavenumbers in cm<sup>-1</sup>, with the 1 $\sigma$  uncertainties of the last digits in parentheses. The boldfaced values were observed during this study, whereas the other two wavenumbers are taken from ref. 36. Relying on  $p_1$  and  $p_2$ , two independent estimates can be derived for the (0 1 0)<sub>42,3</sub> relative energy, which are presented in the violet box of panel **a**. In fact,  $p_1$  and  $p_2$  form a 12-membered cycle with a discrepancy of  $5.1(50) \times 10^{-7}$  cm<sup>-1</sup> [15.4(151) kHz]. For technical details on the determination of relative energies and discrepancies, Eqs. (1–5). Panel **b** presents two typical Lamb dips, a regular and an inverted profile, recorded with our NICE-OHMS apparatus. To aid their comparison, both spectra are mapped onto the  $(I_{\min} - I) / I_{\min}$  intensity scale, where  $I$  means the intensity at a detuning point for a particular line, and  $I_{\min}$  is the lowest intensity in the  $\pm 2$  MHz detuning region. As documented in ref. 41, inverted profiles occur for transitions with large ( $>0.1$  s<sup>-1</sup>) Einstein-A coefficients.

observations are needed, for which some target lines might fall outside the ranges of the three lasers of this study.

Owing to the efficiency of the network approach, the benchmark-quality predicted line lists of H<sub>2</sub><sup>16</sup>O/H<sub>2</sub><sup>18</sup>O include 4.8/4.2 times more transitions with high ( $S \geq 10^{-25}$  cm molecule<sup>-1</sup>) intensities than the set of direct Lamb-dip measurements. These large multiplication factors justify our efforts to achieve overall connectivity within the *ortho/para* subnetworks. The new benchmark line lists of the two water isotopologues encompass a considerable number of frequency standards, suitable for the calibration of Doppler-broadened spectra (note that our previous H<sub>2</sub><sup>16</sup>O line list<sup>36</sup> has already been invoked in ref. 49 to report

corrected Fourier-transform line positions). Furthermore, those transitions falling into the mid-infrared bandwidth of the James Webb Space Telescope, 5–28.5  $\mu$ m (350–2000 cm<sup>-1</sup>), would be optimal targets for tracing water isotopologues in exoplanetary atmospheres and improve our understanding of masers within the bending fundamental<sup>50,51</sup>.

## Methods

**Theory.** The SNAPS approach<sup>36</sup> employed in this study proved to be ideal to maximize the utility of results extracted from precision-spectroscopy measurements<sup>40,41</sup>, where the so-called primary line parameters (wavenumbers, intensities, and

Einstein-*A* coefficients) are restricted to narrow ranges. The SNAPS procedure consists of the following steps: (a) construction of paths and cycles from accurate literature transitions, augmented with target lines in specific intervals of the primary line parameters, (b) detection of the target transitions, and (c) analysis of the paths and cycles comprising the old and new lines. For the selection of the targeted H<sub>2</sub><sup>16</sup>O and H<sub>2</sub><sup>18</sup>O lines, the primary line parameters were taken from ref. 42. To avoid extreme scanning times, refined initial wavenumbers coming from  $\Lambda$ -correction schemes<sup>40</sup> were provided for transitions with  $S < 10^{-25}$  cm molecule<sup>-1</sup>.

During step (c), an accurate energy difference is calculated for each path between its starting and ending states by using the Ritz principle in a sequential fashion:

$$E_{j_{L+1}} - E_{j_1} = \sum_{i=1}^L s_i \tilde{\nu}_{i_i}, \quad (1)$$

which is characterized with a well-defined  $1\sigma$  uncertainty,

$$u(E_{j_{L+1}} - E_{j_1}) = \sqrt{\sum_{k=1}^L u^2(\tilde{\nu}_{i_k})}. \quad (2)$$

In these formulas, (i)  $L$  designates the path length, (ii)  $i_1, i_2, \dots, i_L$  and  $j_1, j_2, \dots, j_{L+1}$  correspond to the indices of transitions and states occurring on this path, respectively, (iii)  $E_n$  indicates the energy of the  $n$ th state, (iv)  $\tilde{\nu}_m$  and  $u(\tilde{\nu}_m)$  are the wavenumber of the  $m$ th transition and its  $1\sigma$  uncertainty, respectively, and (v)  $s_{i_k}$  is the sign pertaining to the  $i_k$ th line of this path. The  $s_{i_k}$  signs are chosen such that the energies of the intermediate states,  $E_{j_k}$  with  $1 < k \leq L$ , will not appear in Eq. (1). When the starting state of this path coincides with the lowest-energy state of a particular nuclear-spin isomer, then the predicted energy difference is identical to the relative energy of the ending state.

If the path behind Eqs. (1) and (2) is extended with an extra transition, indexed with  $i_{L+1}$ , a cycle is obtained. In this case, there are two predictions for  $E_{j_{L+1}} - E_{j_1}$ , and their unsigned difference is the discrepancy of the underlying cycle,

$$D = \left| \sum_{k=1}^{L+1} s_k \tilde{\nu}_{i_k} \right|, \quad (3)$$

associated with a definitive  $1\sigma$  uncertainty,

$$u(D) = \sqrt{\sum_{k=1}^{L+1} u^2(\tilde{\nu}_{i_k})}. \quad (4)$$

To decide whether the discrepancy is within an acceptable limit, a Student-*t* test can be performed, which prescribes

$$D \leq t_{\text{crit}} u(D), \quad (5)$$

whereby  $t_{\text{crit}}$  means the critical Student-*t* factor ( $t_{\text{crit}} \approx 2$  for 95 % significance level). When a cycle does not satisfy Eq. (5), there is a conflict among the transitions of this cycle (note that multiple measurements can be viewed as two-membered trivial cycles). Hence, this compatibility criterion makes cycles useful for the verification of the internal accuracy of ultraprecise SNs.

**Experiment.** As to the most important instrumental aspects of this study, the majority of the lines within the range of Laser II were interrogated with a NICE-OHMS setup described in refs. 26,36, and 41. In this setup, an infrared diode laser is operated at 1.4  $\mu\text{m}$ , combined with a high-finesse cavity. This laser is modulated at 305 MHz to yield side-band signals and at 20 MHz for its lock into the cavity via a Pound-Drever-Hall stabilization scheme. Due to the presence of highly reflective mirrors, of which

one is dithered at a low (405 Hz) frequency, the intracavity power can be varied up to 150 W. The spectroscopic signal is demodulated by a lock-in system (Zurich Instruments; HF2LI). An optical frequency comb, disciplined by a cesium atomic clock, is also utilized in this apparatus to stabilize the infrared laser and to reach sub-kHz precision on the frequency scale.

For the rest of the Lamb-dip measurements, another NICE-OHMS spectrometer was deployed, which was actually designed to probe a very weak ( $A = 1.3 \times 10^{-7}$  s<sup>-1</sup> and  $S = 1.6 \times 10^{-27}$  cm molecule<sup>-1</sup>) quadrupole line of H<sub>2</sub> under saturation<sup>32</sup>. The main features of the latter setup are as follows: (i) temperature control in the optical cavity, down to the mK level, avoiding background noise caused by residual amplitude modulation in the measured signal, (ii) efficient vibration isolation, ensuring high stability and accuracy during long-term averaging of multiple scans, and (iii) greatly improved sensitivity, characterized by a finesse of 350 000, a maximum intracavity laser power up to 10 kW, a beam waist of 542  $\mu\text{m}$ , and a mirror reflectivity of  $R > 0.99999$ . This advanced setup proved to be sensitive enough to yield a minimum uncertainty of 1.9 kHz for the detected lines and record an extremely weak ( $A = 1.7 \times 10^{-2}$  s<sup>-1</sup> and  $S = 4.9 \times 10^{-28}$  cm molecule<sup>-1</sup>) transition for H<sub>2</sub><sup>16</sup>O.

The uncertainties of the line positions reported in this study are affected by numerous experimental factors arising mostly from homogeneous broadening processes<sup>52</sup>. To determine the  $1\sigma$  uncertainty of an observed frequency,  $\delta$ , the following uncertainty budget is applied:

$$\delta = \sqrt{\delta_{\text{stat}}^2 + \delta_{\text{day}}^2 + \delta_{\text{pow}}^2 + \delta_{\text{pres}}^2}, \quad (6)$$

whereby  $\delta_{\text{stat}}$ ,  $\delta_{\text{day}}$ ,  $\delta_{\text{pow}}$ , and  $\delta_{\text{pres}}$  are the statistical, day-to-day, power-shift, and pressure-shift uncertainties, respectively. These individual uncertainty terms are also listed in Supplementary Data 1 for all lines detected during the present study.

### Data availability

The experimental and calculated data of this study are provided as a compressed Supplementary Data 1 file, both for H<sub>2</sub><sup>16</sup>O and H<sub>2</sub><sup>18</sup>O. This compressed file contains old and new high-precision lines, high-accuracy predicted line lists, highly-accurate relative energies, basic cycles built upon the new and old high-precision measurements, the connection lists of the experimental spectroscopic networks considered, the degree distributions of the states, and the high-accuracy absolute energies of the hubs. Data behind Figs. 1–4 can also be found in Supplementary Data 1.

### Code availability

The computer codes used for the selection of target lines are available, upon reasonable request, from the second corresponding author (AGC).

Received: 23 October 2023; Accepted: 8 January 2024;

Published online: 16 February 2024

### References

- Newman, M. E. J. *Networks*, Oxford University Press, Oxford, (2010).
- Barabási, A.-L. & Albert, R. Emergence of scaling in random networks. *Science* **286**, 509–512 (1999).
- Fortunato, S. & Newman, M. E. J. 20 years of network community detection. *Nat. Phys.* **18**, 848–850 (2022).
- Newman, M. E. J. Communities, modules and large-scale structure in networks. *Nat. Phys.* **8**, 25–31 (2012).
- Young, J.-G., Valdovinos, F. S. & Newman, M. E. J. Reconstruction of plant-pollinator networks from observational data. *Nat. Commun.* **12**, 3911 (2021).
- Reyna, M. A. et al. Pathway and network analysis of more than 2500 whole cancer genomes. *Nat. Commun.* **11**, 729 (2020).

- Bazinet, V. et al. Assortative mixing in micro-architecturally annotated brain connectomes. *Nat. Commun.* **14**, 2850 (2023).
- Firth, J. A. et al. Using a real-world network to model localized COVID-19 control strategies. *Nat. Med.* **26**, 1616–1622 (2020).
- Kojaku, S., Hébert-Dufresne, L., Mones, E., Lehmann, S. & Ahn, Y.-Y. The effectiveness of backward contact tracing in networks. *Nat. Phys.* **17**, 652–658 (2021).
- Newman, M. E. J. Assortative mixing in networks. *Phys. Rev. Lett.* **89**, 208701 (2002).
- Broido, A. D. & Clauset, A. Scale-free networks are rare. *Nat. Commun.* **10**, 1017 (2022).
- Császár, A. G., Czako, G., Furtenbacher, T. & Mátyus, E. An active database approach to complete spectra of small molecules. *Annu. Rep. Comput. Chem.* **3**, 155–176 (2007).
- Császár, A. G. & Furtenbacher, T. Spectroscopic networks. *J. Mol. Spectrosc.* **266**, 99–103 (2011).
- Ritz, W. On a new law of series spectra. *Astrophys. J.* **28**, 237–243 (1908).
- Gordon, I. E. et al. The HITRAN2020 molecular spectroscopic database. *J. Quant. Spectrosc. Radiat. Transf.* **276**, 107949 (2022).
- Furtenbacher, T., Árendás, P., Mellau, G. & Császár, A. G. Simple molecules as complex systems. *Sci. Rep.* **4**, 4654 (2014).
- Árendás, P., Furtenbacher, T. & Császár, A. G. On spectra of spectra. *J. Math. Chem.* **54**, 806–822 (2016).
- Császár, A. G., Furtenbacher, T. & Árendás, P. Small molecules – big data. *J. Phys. Chem. A* **120**, 8949–8969 (2016).
- Tóbiás, R., Furtenbacher, T. & Császár, A. G. Cycle bases to the rescue. *J. Quant. Spectrosc. Radiat. Transf.* **203**, 557–564 (2017).
- Árendás, P., Furtenbacher, T. & Császár, A. G. From bridges to cycles in spectroscopic networks. *Sci. Rep.* **10**, 1–13 (2020).
- Tóbiás, R., Bérczi, K., Szabó, C. & Császár, A. G. autoECART: automatic energy conservation analysis of rovibronic transitions. *J. Quant. Spectrosc. Radiat. Transf.* **272**, 107756 (2021).
- Ma, L.-S., Ye, J., Dubé, P. & Hall, J. L. Ultrasensitive frequency-modulation spectroscopy enhanced by a high-finesse optical cavity: theory and application to overtone transitions of C<sub>2</sub>H<sub>2</sub> and C<sub>2</sub>HD. *J. Opt. Soc. Am. B* **16**, 2255–2268 (1999).
- Foltynowicz, A., M. Schmidt, F., Ma, W. & Axner, O. Noise-immune cavity-enhanced optical heterodyne molecular spectroscopy: Current status and future potential. *Appl. Phys. B* **92**, 313–326 (2008).
- Twagiryazu, S., Cich, M. J., Sears, T. J., McRaven, C. P. & Hall, G. E. Frequency-comb referenced spectroscopy of  $\nu_4$ - and  $\nu_5$ -excited hot bands in the 1.5  $\mu\text{m}$  spectrum of C<sub>2</sub>H<sub>2</sub>. *J. Mol. Spectrosc.* **316**, 64–71 (2015).
- Gatti, D. et al. Comb-locked Lamb-dip spectrometer. *Sci. Rep.* **6**, 27183 (2016).
- Cozijn, F. M. J., Dupré, P., Salumbides, E. J., Eikema, K. S. E. & Ubachs, W. Sub-Doppler frequency metrology in HD for tests of fundamental physics. *Phys. Rev. Lett.* **120**, 153002 (2018).
- Reed, Z., Drouin, B., Long, D. & Hodges, J. Molecular transition frequencies of CO<sub>2</sub> near 1.6  $\mu\text{m}$  with kHz-level uncertainties. *J. Quant. Spectrosc. Radiat. Transf.* **271**, 107681 (2021).
- Maity, A., Maithani, S. & Pradhan, M. Cavity ring-down spectroscopy: recent technological advancements, techniques, and applications. *Anal. Chem.* **93**, 388–416 (2021).
- Fasci, E., Gravina, S., Porzio, G., Castrillo, A. & Gianfrani, L. Lamb-dip cavity ring-down spectroscopy of acetylene at 1.4  $\mu\text{m}$ . *New J. Phys.* **23**, 123023 (2021).
- Sinhal, M., Johnson, A. & Willitsch, S. Frequency stabilisation and SI tracing of mid-infrared quantum-cascade lasers for precision molecular spectroscopy. *Mol. Phys.* **121**, e2144519 (2022).
- Aiello, R. et al. Absolute frequency metrology of buffer-gas-cooled molecular spectra at 1 kHz accuracy level. *Nat. Commun.* **13**, 7016 (2022).
- Cozijn, F. M. J., Diouf, M. L. & Ubachs, W. Lamb dip of a quadrupole transition in H<sub>2</sub>. *Phys. Rev. Lett.* **131**, 073001 (2023).
- Jansen, P., Xu, L.-H., Kleiner, I., Ubachs, W. & Bethlem, H. L. Methanol as a sensitive probe for spatial and temporal variations of the proton-to-electron mass ratio. *Phys. Rev. Lett.* **106**, 100801 (2011).
- Salumbides, E. J. et al. Bounds on fifth forces from precision measurements on molecules. *Phys. Rev. D* **87**, 112008 (2013).
- Cazzoli, G., Puzzarini, C. & Lapinov, A. Precise laboratory frequencies for the  $J \leftarrow J-1$  ( $J = 1, 2, 3, 4$ ) rotational transitions of <sup>13</sup>CO. *Astrophys. J.* **611**, 615 (2004).
- Tóbiás, R. et al. Spectroscopic-network-assisted precision spectroscopy and its application to water. *Nat. Commun.* **11**, 1708 (2020).
- Kukolich, S. G. Measurement of the molecular  $g$  values in H<sub>2</sub>O and D<sub>2</sub>O and hyperfine structure in H<sub>2</sub>O. *J. Chem. Phys.* **50**, 3751–3755 (1969).
- Golubiatnikov, G. Y., Markov, V. N., Guarnieri, A. & Knochel, R. Hyperfine structure of H<sub>2</sub><sup>16</sup>O and H<sub>2</sub><sup>18</sup>O measured by Lamb-dip technique in the 180–560 GHz frequency range. *J. Mol. Spectrosc.* **240**, 251–254 (2006).
- Cazzoli, G., Puzzarini, C., Harding, M. E. & Gauss, J. The hyperfine structure in the rotational spectrum of water: Lamb-dip technique and quantum-chemical calculations. *Chem. Phys. Lett.* **473**, 21–25 (2009).
- Diouf, M. L. et al. Network-based design of near-infrared Lamb-dip experiments and the determination of pure rotational energies of H<sub>2</sub><sup>18</sup>O at kHz accuracy. *J. Phys. Chem. Ref. Data* **50**, 023106 (2021).
- Diouf, M. L. et al. Ultraprecise relative energies in the (2 0 0) vibrational band of H<sub>2</sub><sup>16</sup>O. *Mol. Phys.* **120**, e2050430 (2022).
- Furtenbacher, T. et al. The W2020 database of validated rovibrational experimental transitions and empirical energy levels of water isotopologues. Part II. H<sub>2</sub><sup>17</sup>O and H<sub>2</sub><sup>18</sup>O with an update to H<sub>2</sub><sup>16</sup>O. *J. Phys. Chem. Ref. Data* **49**, 043103 (2020).
- Grechko, M. et al. State-selective spectroscopy of water up to its first dissociation limit. *J. Chem. Phys.* **131**, 221105 (2009).
- Miani, A. & Tennyson, J. Can *ortho-para* transitions for water be observed? *J. Chem. Phys.* **120**, 2732–2739 (2004).
- Yachmenev, A., Yang, G., Zak, E., Yurchenko, S. & Küpper, J. The nuclear-spin-forbidden rovibrational transitions of water from first principles. *J. Chem. Phys.* **156**, 204307 (2022).
- Kassi, S., Stoltmann, T., Casado, M., Daeron, M. & Campargue, A. Lamb dip CRDS of highly saturated transitions of water near 1.4  $\mu\text{m}$ . *J. Chem. Phys.* **148**, 054201 (2018).
- Chen, J. et al. Absolute frequencies of water lines near 790 nm with 10<sup>-11</sup> accuracy. *J. Quant. Spectrosc. Radiat. Transf.* **205**, 91–95 (2018).
- Kassi, S., Lauzin, C., Chaillot, J. & Campargue, A. The (2–0) R(0) and R(1) transition frequencies of HD determined to a 10<sup>-10</sup> relative accuracy by Doppler spectroscopy at 80 K. *Phys. Chem. Chem. Phys.* **24**, 23164–23172 (2022).
- Karlovetz, E., Mikhailenko, S., Koroleva, A. & Campargue, A. Water vapor absorption spectroscopy and validation tests of databases in the far-infrared (50–720 cm<sup>-1</sup>). Part 2: H<sub>2</sub><sup>17</sup>O and HD<sup>17</sup>O. *J. Quant. Spectrosc. Radiat. Transf.* **291**, 108829 (2023).
- Chen, P., Pearson, J. C., Pickett, H. M., Matsuura, S. & Blake, G. A. Submillimeter-wave measurements and analysis of the ground and  $\nu_2 = 1$  states of water. *Astrophys. J. Suppl. S.* **128**, 371–385 (2000).
- Yu, S. et al. Measurement and analysis of new terahertz and far-infrared spectra of high temperature water. *J. Mol. Spectrosc.* **279**, 16–25 (2012).
- Letokhov, V. S. & Chebotayev, V. P. *Nonlinear Laser Spectroscopy*, Springer-Verlag, Berlin, (1977).
- Matsushima, F., Tomatsu, N., Nagai, T., Moriawaki, Y. & Takagi, K. Frequency measurement of pure rotational transitions in the  $\nu_2 = 1$  state of H<sub>2</sub>O. *J. Mol. Spectrosc.* **235**, 190–195 (2006).
- Yu, S., Pearson, J. C. & Drouin, B. J. Terahertz spectroscopy of water in its second triad. *J. Mol. Spectrosc.* **288**, 7–10 (2013).

## Acknowledgements

The research received funding from LASERLAB-EUROPE (grant no. 654148), a European Unions Horizon 2020 research and innovation programme. The work performed in Budapest received support from the NKFIH grants K138233 and PD145972. At the Amsterdam side, support was obtained from a NWO program (16MYSTP).

## Author contributions

Conducted the experiments and resolved the lines: M.L.D. and F.M.J.C.; selected the list for the experiments, evaluated the resolved lines, and created the figures: R.T.; designed and supervised the research: A.G.C. and W.U.; all authors discussed the results and wrote the manuscript.

## Funding

Open access funding provided by Eötvös Loránd University.

## Competing interests

The authors declare no competing interests.

## Additional information

**Supplementary information** The online version contains supplementary material available at <https://doi.org/10.1038/s42004-024-01103-8>.

**Correspondence** and requests for materials should be addressed to Wim Ubachs or Attila G. Császár.

**Peer review information** *Communications Chemistry* thanks Andrey Yachmenev and the other anonymous reviewers for their contribution to the peer review of this work.

**Reprints and permission information** is available at <http://www.nature.com/reprints>

**Publisher's note** Springer Nature remains neutral with regard to jurisdictional claims in published maps and institutional affiliations.





**Open Access** This article is licensed under a Creative Commons Attribution 4.0 International License, which permits use, sharing, adaptation, distribution and reproduction in any medium or format, as long as you give appropriate credit to the original author(s) and the source, provide a link to the Creative Commons license, and indicate if changes were made. The images or other third party material in this article are included in the article's Creative Commons license, unless indicated otherwise in a credit line to the material. If material is not included in the article's Creative Commons license and your intended use is not permitted by statutory regulation or exceeds the permitted use, you will need to obtain permission directly from the copyright holder. To view a copy of this license, visit <http://creativecommons.org/licenses/by/4.0/>.

© The Author(s) 2024